Journal of Alloys and Compounds 947 (2023) 169430

Contents lists available at ScienceDirect

Journal of Alloys and Compounds

journal homepage: www.elsevier.com/locate/jalcom

Research Article

# Synthesis and characterization of dense, rare-earth based high entropy fluorite thin films

Mohana V. Kante [a], Horst Hahn [a,b], Subramshu S. Bhattacharya [c], Leonardo Velasco [d,*]

[a] Institute of Nanotechnology, Karlsruhe Institute of Technology, 76344 Eggenstein-Leopoldshafen, Germany
[b] University of Oklahoma, Chemical, Biological and Materials Engineering, Norman, OK 73019, USA
[c] NFMTC, Department of Metallurgical and Materials Engineering, Indian Institute of Technology Madras, Chennai 600036, India
[d] Universidad Nacional de Colombia sede de La Paz, Km 9 via Valledupar, La Paz, 202010 Cesar, Colombia

ARTICLE INFO

*Article history:*
Received 25 November 2022
Received in revised form 16 February 2023
Accepted 24 February 2023
Available online 28 February 2023

*Keywords:*
High entropy oxides
Fluorite structure
Dense materials
Thin films

ABSTRACT

High entropy oxides (HEOs) with 5 or more cations in equimolar proportions that result in a phase-pure material, are a new class of materials attracting a lot of attention in recent years. HEOs exhibit interesting optical, electrochemical, magnetic and catalytic properties. To get a comprehensive understanding of the physics behind the complex interactions taking place in these materials, it is important to evaluate the material in (near-fully) dense forms, such as pellets or thin films. The fluorite structured high entropy oxide, $(CeLaSmPrY)O_{2-x}$ has been investigated only in the powder form and there are no studies on the dense form of fluorite $(CeLaSmPrY)O_{2-x}$. One of the main reasons is that $(CeLaSmPrY)O_{2-x}$ undergoes a structural transition from fluorite to bixbyite (at 1000 °C) and typically temperatures above the transition (> 1200 °C) are required for achieving high densities via conventional sintering. In this study, we synthesize dense films of fluorite structured $(CeLaSmPrY)O_{2-x}$ by sol-gel as well as pulsed laser deposition processes. The films synthesized via sol-gel process exhibit equiaxed grains and polycrystalline morphology, whereas columnar and epitaxial films are obtained using pulsed laser deposition. Thus, microstructural tuning of dense fluorite $(CeLaSmPrY)O_{2-x}$ films has been demonstrated while maintaining the basic characteristics of the HEO as observed in the powder form, therefore, paving the way towards more comprehensive studies for possible applications.



## 1. Introduction

In recent years, equiatomic or near-equiatomic multicomponent oxides with 5 or more principal cations have emerged as a novel and important class of ceramics with interesting functional properties. Despite the chemical complexity, in many cases a single phase has been observed, which is typically attributed to the high configurational entropy (> 1.6 R), that offsets the enthalpic contribution in the Gibbs free energy equation [1]. Consequently, such phase-pure multicomponent oxide systems are termed as high entropy oxides (HEO) or compositionally complex materials (CCM). The first HEO reported was a rocksalt structured (CoCuMgNiZn)O synthesized by Rost et.al. [2]. Since then, various HEOs with rocksalt structure [2], fluorite structure [3–5], spinel structure [6–8], perovskite structure [9,10], pyrochlore structure [11–13], and layered structure [14] have been synthesized. Many of these HEOs, show enhanced catalytic activity [15], electrochemical storage [16], and magnetic properties [17] among other exciting properties[18]. The usual synthesis techniques for HEOs like reverse co-precipitation, flame spray pyrolysis, nebulized spray pyrolysis, solution combustion, solid-state reaction, mechanochemistry, etc. [2,19–23] result in the product being in the powder form which are then characterized for their structural and functional properties. On the other hand, most actual applications require the material to be in bulk (near-fully dense) or compact forms. There are only a few studies on the preparation of dense bulk samples or thin films of HEOs using synthesis techniques like conventional sintering, spark plasma sintering, and pulsed laser deposition [24–26]. The main difficulty lies in making bulk dense structures while retaining the physical and chemical characteristics observed in the powder form.

Rare earth (RE) oxides are known for their catalytic activity, oxygen ionic conductivity and optical properties [27–29]. A key role to obtain such interesting properties arise from the presence of oxygen vacancies [30,31]. In fluorite structured rare earth-based oxide systems, the addition of cations with a +3 oxidation state results in a charge deficiency which is compensated by the creation of

* Corresponding author.
*E-mail address:* lvelascoe@unal.edu.co (L. Velasco).

https://doi.org/10.1016/j.jallcom.2023.169430

oxygen vacancies. (CeLaSmPrY)$O_{2-x}$ is a rare-earth-based HEO which has three +3 cations and their presence in high fractions can result in a substantial concentration of oxygen vacancies. Initial investigations by Djenadic et.al. demonstrated that (CeLaSmPrY)$O_{2-x}$ exhibits both fluorite and bixbyite structures depending on the annealing temperature [32]. However, when the fluorite structure transforms to bixbyite at a temperature > 1000°C, the concentration of oxygen vacancies reduces, thereby lowering the efficacy of the material for possible applications. For (CeLaSmPrY)$O_{2-x,}$ the optical properties have been investigated in detail and a low band gap of 2.06 eV has been observed [23] in the powder form. However, the properties in bulk form like a sintered pellet or a thin film are yet to be explored. Pellets of high density fabricated by the conventional sintering process can only be achieved at temperatures above 1000°C [33–35], which in this case would be greater than the (fluorite to bixbyite) transformation temperature. Then, the fluorite structure would change to a bixbyite resulting in a lower oxygen vacancy concentration.

In view of the restrictions on the synthesis and sintering temperature of a fluorite structured (CeLaSmPrY)$O_{2-x}$, it is imperative to explore other techniques that allow the fabrication of a dense structure at sufficiently low temperatures. Here, in this study we present two possible ways to synthesize dense fluorite structured (CeLaSmPrY)$O_{2-x}$ thin films with three different morphologies using sol-gel and pulsed laser deposition methods. X-ray diffraction (XRD) and transmission electron microscopy (TEM) were employed to investigate the morphology and structure of the films. Electron energy loss spectroscopy (EELS) and X-ray photoemission spectroscopy (XPS) were employed to analyze the oxidation states of the different cations. Additionally, UV–vis spectroscopy was conducted to determine the optical band gap.

## 2. Methods

For Pulsed Laser Deposition (PLD), a target was fabricated by conventional sintering of nanoparticle powders of (CeLaSmPrY)$O_{2-x}$, synthesized by reverse co-precipitation (RCP). $Ce(NO_3)_3{\cdot}6\ H_2O$ (ALFA AESAR, 99.9 %), $La(NO_3)_3{\cdot}6\ H_2O$ (Sigma-Aldrich, 99.9 %), $Pr(NO_3)_3{\cdot}6\ H_2O$ (ABCR, 99.9 %), $Sm(NO_3)_3{\cdot}6\ H_2O$ (ABCR, 99.9 %) and $Y(NO_3)_3{\cdot}6\ H_2O$ (ABCR, 99.9 %) nitrate salts were dissolved in water and used as precursors for RCP. The precursor solution was added dropwise to 28 % ammonia solution (Sigma-Aldrich) resulting in the precipitation of metal hydroxides. The precipitates were dried and heat-treated at 750°C for 6 h. The heat treated powder (~10 g) was pressed at 300 MPa and subsequently sintered at 1000°C for 12 h in air to form the (CeLaSmPrY)$O_{2-x}$ target for PLD. Fabrication of films by PLD was carried out on Si (100) substrates (referred to as PLD-Si) and YSZ (111) substrates (referred to as PLD-YSZ). The Si substrates were ultrasonically cleaned in acetone and isopropanol before deposition while YSZ was used in the as-received condition. A Surface systems + technology PLD equipped with KrF laser with a wavelength of 248 nm was used. PLD was carried out with a fluence of 1.6 J/cm$^2$, a frequency of 1 Hz at 0.05 mbar oxygen pressure and the substrate temperature was 750 °C. The distance between target and film was 2.5 cm.

The films obtained by sol-gel processing (referred to as SG) were synthesized by the Pechini method. $Ce(NO_3)_3{\cdot}6\ H_2O$ (ALFA AESAR, 99.9 %), $La(NO_3)_3{\cdot}6\ H_2O$ (Sigma-Aldrich, 99.9 %), $Pr(NO_3)_3{\cdot}6\ H_2O$ (ABCR, 99.9 %), $Sm(NO_3)_3{\cdot}6\ H_2O$ (ABCR, 99.9 %) and $Y(NO_3)_3{\cdot}6\ H_2O$ (ABCR, 99.9 %) nitrate salts were dissolved in 2-methoxyethanol solution (Sigma-Aldrich, 99.0 %) and stirred until all the salts dissolved and a clear solution formed. Citric acid and ethylene glycol, used as chelating and polymerizing agents, were added to the solution such that the ratio between metal ions, citric acid and ethylene glycol was 1:2:4 at a metal ion concentration of 0.2 M. The solution was stirred at 80°C until it became half in volume following which 2-methoxyethanol was added to make up for the lost volume. The precursor solution was then spin-coated onto the cleaned Si(100) substrate at 6000 rpm for 60 s and dried on a hot plate at 300 °C. Once the film dried another round of spin coating was carried out followed by drying at 300 °C. 5 such cycles of coating were carried out and the final film annealed at 750 °C for 3 hrs.

The crystal structure of the films was investigated by X-ray diffraction (XRD) using Grazing Incidence X-Ray Diffraction (GIXRD) and High-resolution X-Ray Diffraction (HRXRD). GIXRD was conducted in a Bruker D8 X-ray Diffractometer equipped with a Cu X-ray source and a Lynxeye detector. The GIXRD measurements were performed over a two-theta range of 10°– 71° with the source being fixed at 4°. Bruker AXS X-ray diffractometer with a Cu source was utilized for HRXRD over a two-theta range of 20°– 80° while fixing the source at 14.85° on the film deposited on the YSZ substrate to study the epitaxial nature of the film.

The surface morphologies of the films were investigated via Scanning Electron Microscopy (SEM) with a Gemini Leo 1530 SEM, at an accelerating voltage of 5 kV and a working distance of 8.5 mm. The film's cross-section was investigated by Transmission Electron Microscopy (TEM). An FEI strata 400 Focus Ion Beam system was used to extract the TEM lamella with a platinum layer coating on top of the film to avoid degradation and damage of the films from the Ga ion beam. A Thermo Fischer Themis-Z transmission electron microscope operating at 300 kV was used to study the cross-section of the film.

The chemical composition and elemental distribution of the films were measured in scanning-TEM (STEM) mode with a Super-X EDX detector. Electron energy loss spectroscopy (EELS) and X-ray photoemission spectroscopy (XPS) were employed to study the oxidation states of the corresponding elements. EELS was carried out in the Thermo Fischer Themis-Z TEM and the spectra were analyzed using Gatan Digital Micrograph 3 software. XPS was carried out using an Omicron XM 1000 MkII with an Al-$K_\alpha$ X-ray (1486.6 eV) source at an operating power of 300 W. The spectra were acquired with a SPECS Phobias 150 spectrometer and the XPS data were analyzed using CASAXPS® software.

UV–vis spectroscopy was conducted in an Agilent Cary 60 device with a remote fiber optic accessory. The samples deposited on Si substrate (SG and PLD-Si) were baseline corrected. The scan was conducted from 1100 to 200 nm with a speed of 600 nm.min$^{-1}$ and reflectance measured. Band gaps were analyzed from Tauc plots using the formula.

$$(\alpha h\nu)^{1/n} = B(h\nu\text{-}E_g)$$

where α is the absorption coefficient, B is a constant, h is Planck's constant, $\nu$ is frequency, and n is the factor that depends on the electronic transition. The absorption coefficient is calculated from the Kubelka-Munk function. Here, we calculated the direct band gap for which n = 1/2. The x-intercept of the linear part of the Tauc plot was taken as the band gap of the material.

## 3. Results and discussion

### 3.1. Structural analysis

XRD patterns of (CeLaSmPrY)$O_{2-x}$ films synthesized by PLD (PLD-Si) and sol-gel process (SG) as well as those of the synthesized powder and the PLD-target are depicted in Fig. 1a, while that of PLD-YSZ is shown in high resolution in Fig. 1b. The as-prepared powders have a fluorite structure ($Fm\bar{3}m$), while the structure of the target is bixbyite ($Ia\bar{3}$), as a result of sintering the target at 1000 °C. In supplementary information Table S1, the chemical composition of the as prepared powders and the target is presented, which shows a small difference of oxygen content being greater for the powders. The XRD

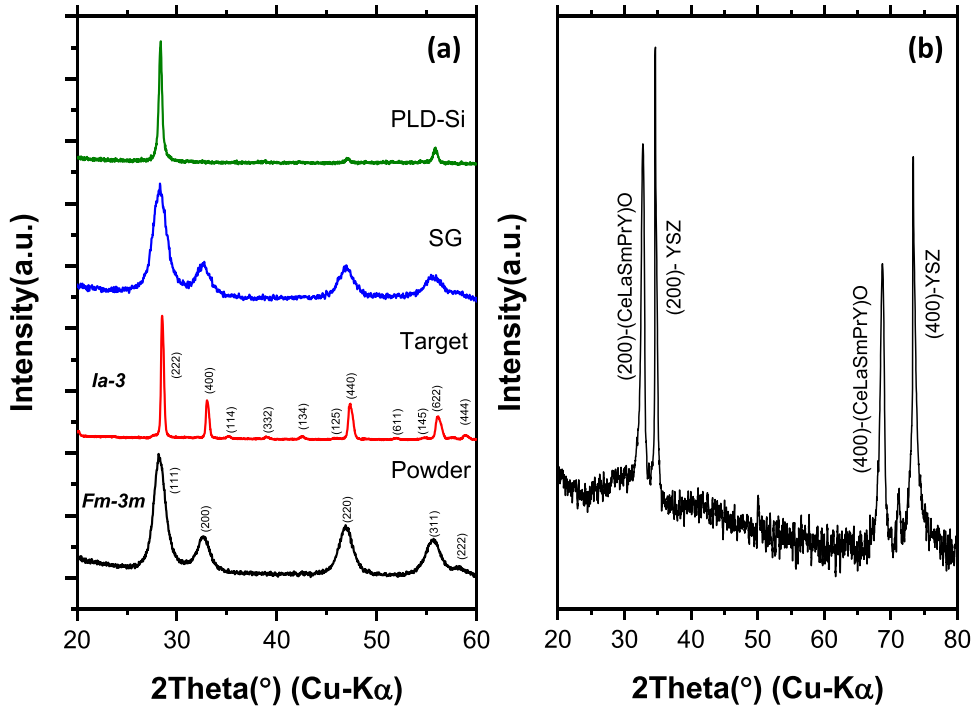


**Fig. 1.** (a) X-ray diffraction pattern of (Ce,La,Sm,Pr,Y)$O_{2-x}$ powder, PLD-target, SG, and PLD-Si. (b) High-resolution XRD of PLD-YSZ sample.

patterns of SG and PLD-Si exhibit polycrystalline fluorite structure, similar to that of the powder XRD pattern. However, the XRD pattern of PLD-Si differs from the powder and SG film, since the relative intensity of the (111) peak is much higher than that of the other peaks, which might be a result of the crystallites in the PLD-Si film being oriented preferentially (111). The HRXRD of the PLD-YSZ sample can be seen in Fig. 1(b) suggesting an epitaxial relationship with a fluorite structure.

The surface morphology of the films was analyzed by scanning electron microscopy (Supplementary information Fig. S1). The images revealed that all the films are dense as well as crack- and pore-free, which is important for the bulk macroscopic properties of the films.

Transmission electron microscopy was performed to further investigate the microstructure of the films (cross-sectional images in Fig. 2). From TEM images of SG (Fig. 2a), it is clear that the polycrystalline film consists of equiaxed grains. The selected area electron diffraction (SAED) pattern (Fig. 2a inset) confirms the crystallinity of the film and the fluorite structure, while the high-resolution TEM image in Fig. 2b shows several crystals with different orientations. The STEM-EDS mapping of SG in Fig. 2c shows that the elements are distributed homogeneously. Fig. 2d and e are TEM micrographs of the PLD-Si sample, clearly consisting of columnar grains along the growth direction of the film. The SAED pattern of PLD-Si shows diffraction spots aligned as concentric rings of the fluorite structure (decorated by dotted lines, see inset in Fig. 2d). STEM chemical mapping of PLD-Si in Fig. 2 f shows a homogenous distribution of the elements. PLD-YSZ did not exhibit columnar grains (Fig. 2 g) even though it was deposited using similar deposition conditions as PLD-Si. Instead, an epitaxial growth can be clearly seen in Fig. 2 h. The SAED pattern also strongly suggests that the film grew epitaxially. STEM chemical mapping images can be seen in Fig. 2i indicating a homogenous distribution of elements for PLD-YSZ.

Overall, the TEM results are in conformity with the XRD results, i.e., all the samples are fluorite structured with the SG sample exhibiting polycrystalline morphology, the PLD-Si sample showing (111) preferred orientation and epitaxial growth in case of PLD-YSZ.

In case of the SG film, the polycrystallinity arose mainly from the synthesis method wherein the heat treatment of the spin-coated film at 750 °C resulted in uniform heating of the sample thereby triggering homogeneous nucleation [36].

Si (100) and YSZ (111) substrates have face-centered cubic lattice parameters (5.44 Å for Si and 5.18 Å for YSZ), which are similar to that of (Ce,La,Pr,Sm,Y)$O_{2-x}$ (5.46 Å). According to several studies [37–39], ceria-based oxides can be deposited epitaxially on both Si and YSZ. However, in the present study PLD-YSZ exhibits epitaxial nature whereas PLD-Si is a film with columnar grains and preferred orientation in the (111) direction. The absence of epitaxy in PLD-Si could be attributed to: (i) the presence of a natural amorphous silicon oxide layer on top of the Si substrate, which can play an important role in epitaxial growth on Si substrates [39]; and (ii) nucleation and preferential growth. During the early stages of PLD, the Si oxide layer acts as a flat surface on which the nuclei grow, depending on substrate temperature (T), along an energetically stable crystallographic plane (in case of FCC structured systems, the (111) plane has the lowest surface energy) [40]. For $0.3\,T_m < T < 0.45\,T_m$ ($T_m$ is the melting point of the film, which in case of RE oxides is typically ~2300°C), a columnar growth is expected in vapor deposition techniques [40]. The PLD-Si was deposited at 750°C which is in the range of $0.3\,T_m < T < 0.45\,T_m$ and as a result, both the substrate temperature and silicon oxide layer on the Si substrate contribute to columnar growth in the (111) PLD-Si film. The PLD-YSZ film and substrate have a similar structure and the difference in lattice parameter ((CeLaSmPrY)$O_{2-x}$ ~ 5.46 Å and YSZ ~ 5.18 Å) might lead to epitaxial growth through the Stranski-Krastanov model [41]. It is noteworthy that although the target is an $Ia\bar{3}$ (bixbyite) structure, the resulting films deposited via PLD have a fluorite structure. This can be explained by the deposition temperature which is 750 °C and presence of an oxygen atmosphere during deposition since the oxygen partial pressure plays an important role in the structure of the films of rare earth oxides in vapor deposition techniques [42–44]. The role played by the oxygen partial pressure can be understood from the transition from bixbyite to

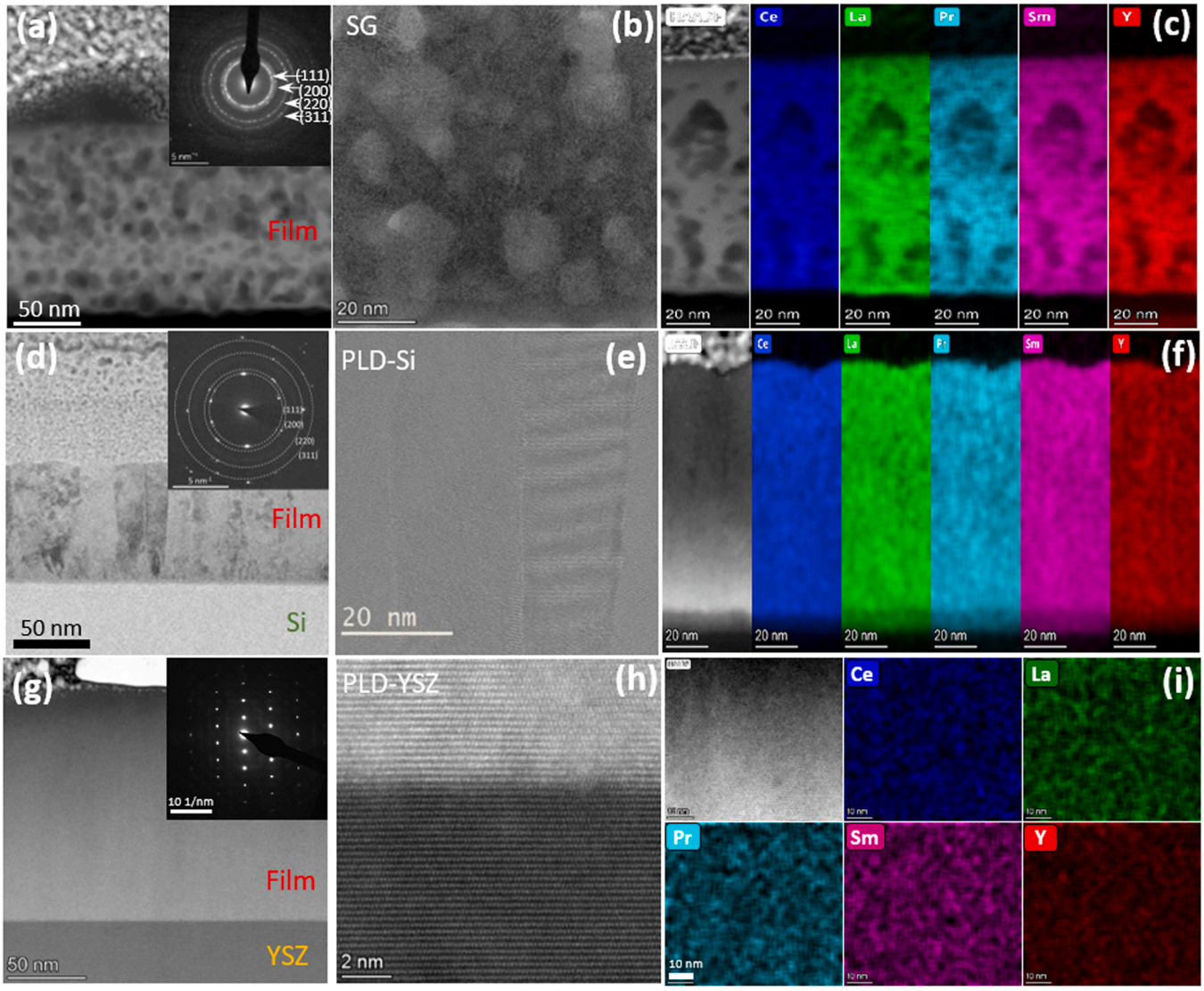


**Fig. 2.** (a) Micrograph of SG cross-section, the inset is the SAED of SG. (b) Zoomed in micrograph of the SG film cross-section. (c) Chemical distribution maps of elements in the SG film. (d) Micrograph of PLD-Si cross-section, the inset is the SAED of PLD-Si. (e) Zoomed in micrograph of the PLD-Si film cross-section. (f) Chemical distribution maps of elements in the PLD-Si film, (g) Micrograph of PLD-YSZ cross-section, the inset is the SAED of PLD-YSZ. (h) Zoomed in micrograph of the PLD-YSZ film cross-section. (i) Chemical distribution maps of elements in the PLD-YSZ film. For elemental chemical composition of the films see Table S2.

fluorite structure as $((Ce,La,Pr,Sm,Y)_2O_3 + 1/2O_2 \rightarrow (Ce,La,Sm,Pr,Y)O_2$ at 750 °C), for which excess oxygen is needed to satisfy the reaction and therefore the structure transformation [45].

### 3.2. Oxidation states

Properties of rare earth oxides strongly depend upon the oxygen vacancies present in the structure [46]. Here, the oxidation states of the cations play a very important role for the existence of anion vacancies. In general, the oxidation state of the cation in stoichiometric fluorite-structured oxides should be +4. Doping with a rare earth cation with a +3 oxidation state results in the formation of oxygen vacancies. In the $(CeLaPrSmY)O_{2-x}$ films with a fluorite structure that has been investigated in this study, the oxidation states of Ce, La, Pr, Sm, and Y determine the concentration of oxygen vacancies. Ce, and Pr exhibit multiple oxidation states with either of them exhibiting both +4 and +3 oxidation states, while the rest of the elements La, Sm, and Y predominantly show a +3 oxidation state. Electron energy loss spectroscopy (EELS) and X-ray photoelectron spectroscopy (XPS) were used to characterize the oxidation states of Ce and Pr. XPS and EELS data of La, Sm, and Y can be seen in the supplementary information (Fig. S2 and Fig. S3), which confirm +3 oxidation states.

### 3.3. The oxidation state of cerium

EELS spectra of SG, PLD-Si, and PLD-YSZ can be seen in Fig. 3(a). Ce exhibits $M_5$ and $M_4$ edges between 880 eV and 920 eV corresponding to electronic transitions from the 3d orbital. The ratio of intensities ($I_{M5}/I_{M4}$) of $M_5$ and $M_4$ peaks is generally utilized to compare the oxidation states of Ce in different systems [45,47,48]. It was observed from the Intensity ratio of $M_5$ and $M_4$ edges that the majority of Ce is in a +4 oxidation state[49,50]. On closer inspection, PLD-Si and PLD-YSZ have almost the same $I_{M5}/I_{M4}$, while the $I_{M5}/I_{M4}$ for the SG is higher, which indicates that the amount of $Ce^{+4}$ in SG is the lowest of the three films. Fig. 3(b-d) shows the XPS spectra of SG, PLD-Si, and PLD-YSZ. Ce exhibits 3d orbital photoemission peaks around 880 eV. In the Ce 3d XPS spectrum, $Ce^{+3}$ exhibits two multiplets of four peaks ($u^0$, $u^I$ and $v^0$, $v^I$) with each multiplet representing transitions from $3d_{3/2}$ and $3d_{5/2}$ of $Ce^{+3}$ respectively, while $Ce^{+4}$ exhibits two multiplets of six peaks (u, $u^{II}$, $u^{III}$ and v,$v^{II}$,$v^{III}$) with each multiplet representing transitions from $3d_{3/2}$ and $3d_{5/2}$ of

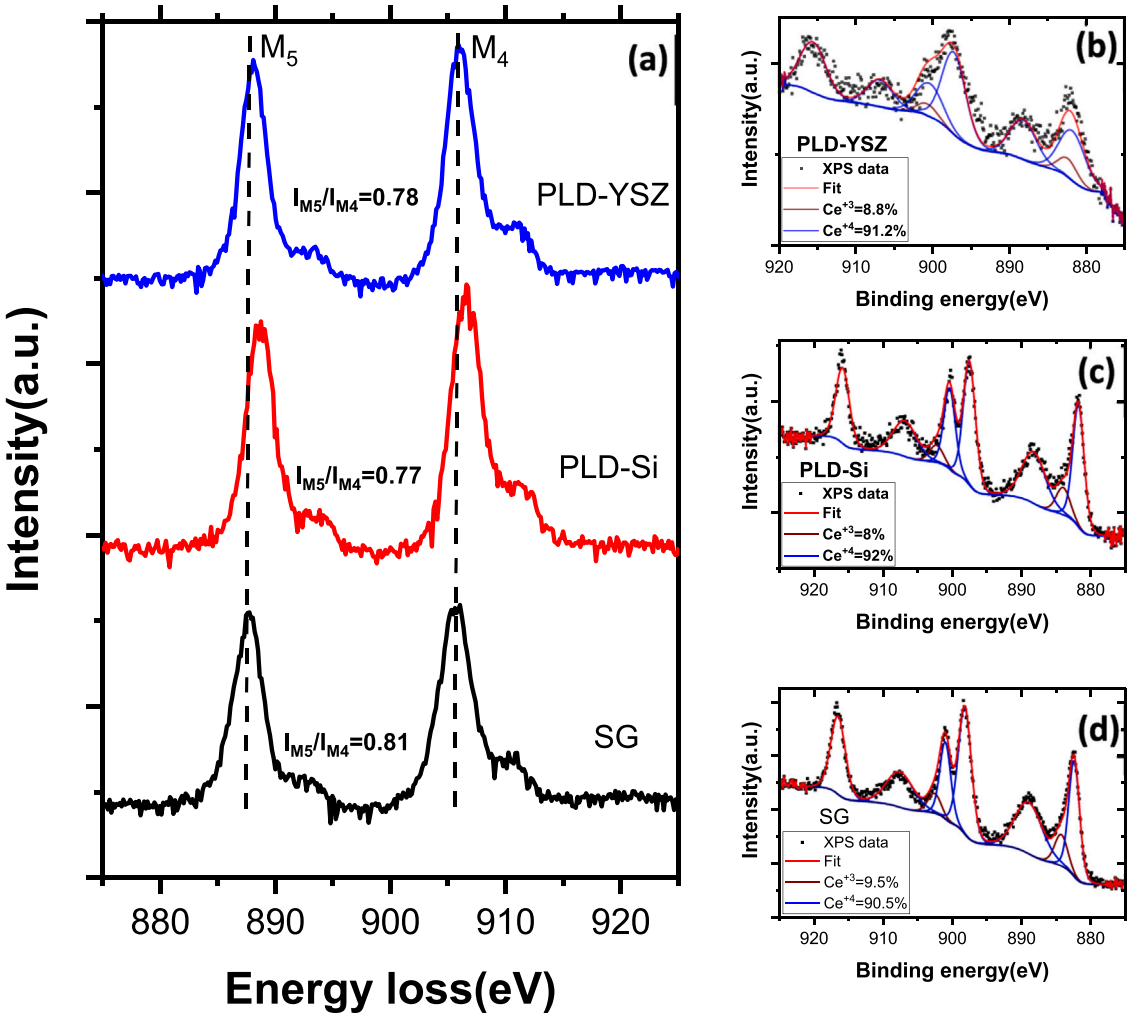


**Fig. 3.** (a)EELS data of Ce 3d transition of SG, PLD-Si and PLD-YSZ (b)(c)(d) XPS data of PLD-YSZ, PLD-Si and SG.

$Ce^{+4}$ ion respectively [51–53]. The XPS data are fitted with $Ce^{+3}$ and $Ce^{+4}$ multiplets following references [51–53] using CASAXPS. The content of $Ce^{+4}$ is interpreted from the fit to be greater than 90 %, with SG having slightly lower $Ce^{+4}$ than the other 2 films. Hence, it could be inferred that most of the Ce in all the films are in the +4 oxidation state.

### 3.4. The oxidation state of praseodymium

EELS data of Pr 3d can be seen in Fig. 4(a). Similar to Ce, Pr exhibits $M_5$ and $M_4$ edges between 930 eV and 970 eV as a result of 3d electronic transitions. The intensity ratio of $M_5$ and $M_4$ edges ($I_{M5}/I_{M4}$) indicates $Pr^{+3}$ to be the dominating species [49]. The PLD-YSZ and SG films have similar $I_{M5}/I_{M4}$ values indicating similar oxidation states, while PLD-Si has the lowest $I_{M5}/I_{M4}$ value. The lower Intensity ratio of PLD-Si implies that PLD-Si has slightly higher $Pr^{+4}$ [45] than the other two films. XPS data of Pr 3d in all the films can be seen in Fig. 4(b). The Pr 3d XPS spectrum can be divided into two multiplets ($a,a^{I},a^{II}$ and $b,b^{I},b^{II}$), t (satellite peak), oxygen Auger line (OKLL) and the positions of the peaks can be seen as dotted lines in Fig. 4(b) [43,54]. a/b and $a^{I}/b^{I}$ are characteristic of transitions from 3d orbitals of both $Pr^{+3}$ and $Pr^{+4}$. However $a^{II}$ and $b^{II}$ appear due to the presence of $Pr^{+4}$ in the system [43,55]. On closer inspection, the $b^{II}$ peak cannot be unambiguously identified in PLD-YSZ and SG samples. However, in the case of PLD-Si, the $b^{II}$ peak can be observed, which suggests the presence of relatively higher amounts of $Pr^{+4}$ in PLD-Si when compared to the other samples. Nevertheless, the difference in the $Pr^{+4}$ content in the three cases appears to be relatively insignificant. Both EELS and XPS analyses suggest that all the films have $Pr^{+3}$ as the predominant species.

### 3.5. Band gap

UV–vis spectroscopy was conducted to investigate the band gap of the films. The band gap values were extracted from the Tauc plots and the results are depicted in Fig. 5. The band gaps of SG, PLD-Si, and PLD-YSZ films are 2.29, 2, and 2.17 eV, respectively. The band gap values of the films are similar to the values observed in the literature for $(Ce,La,Sm,Pr,Y)O_{2-x}$ (~2.06 eV) in powder form[3]. Among the films, PLD-Si has the lowest band gap, which might be attributed to a slightly higher $Pr^{+4}$ content as the presence of $Pr^{+4}$ leads to the formation of an impurity band between Ce 4f and O 2p resulting in lower band gaps in $(Ce,La,Sm,Pr,Y)O_{2-x}$[45,56,57]. Likewise, SG showed the highest band gap as it has the lowest $Pr^{+4}$ content as can be seen from the EELS results (Fig. 4a).

Therefore, it can be seen that all the films have similar crystal structures, oxidation states of the cations, and band gap comparable to those observed for $(Ce,La,Sm,Pr,Y)O_{2-x}$ in the powder form [3,4,32]. However, the morphology of a material can significantly affect the properties and their usage in different applications. For example, rare earth-based oxides are known for their oxygen ion conductivity[58], which are promising candidates as electrolytes in

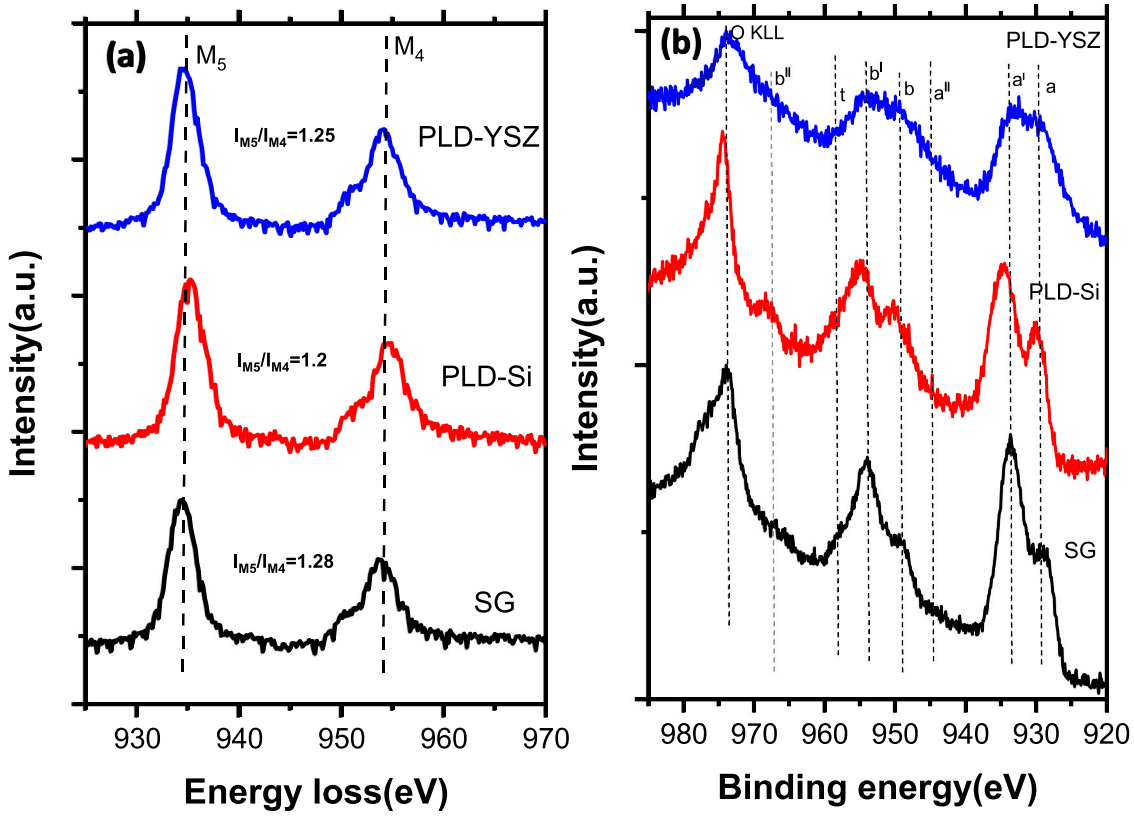


**Fig. 4.** (a) EELS and (b) XPS data of Pr 3d transition of SG, PLD-Si and PLD-YSZ.

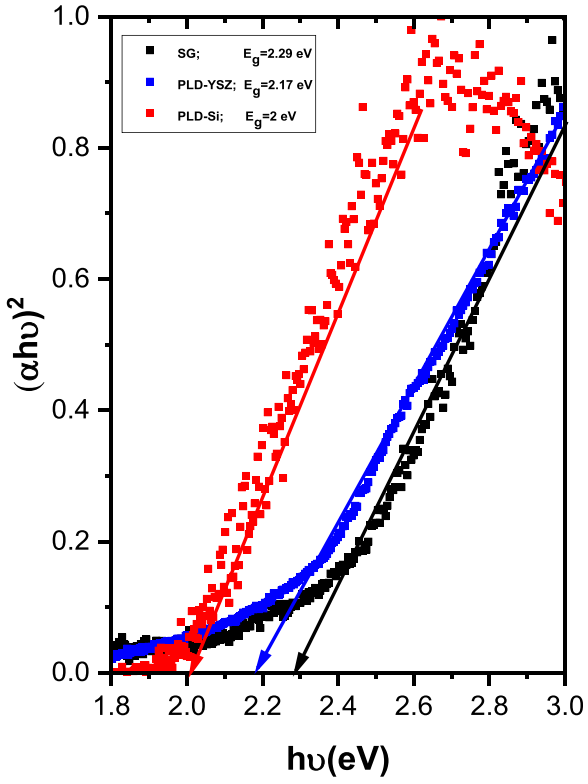


**Fig. 5.** Tauc plot of UV-Vis spectroscopy of SG, PLD-Si and PLD-YSZ films.

solid oxide fuel cell (SOFC) applications. A single crystal or columnar grain-oriented film in the (111) direction, typically has low resistance for cross plane electrolytic conductivity [59–61]. Therefore, the films synthesized by PLD (columnar and epitaxial) could be used as electrolytes in an SOFC. Rare earth-based oxides are well-known for their catalytic activity[62–64] in different reactions and in turn, the films synthesized from the sol-gel process with polycrystalline equiaxed grains are good candidates for catalytic applications.

## 4. Conclusion

In this study, we fabricated temperature sensitive fluorite structured $(CeLaSmPrY)O_{2-x}$ dense films using sol-gel process and pulsed laser deposition. Our methodology could be used to overcome the drawbacks of conventional sintering methods, as $(CeLaSmPrY)O_{2-x}$ converts to bixbyite structure at higher temperatures. We obtained crack- and pore-free dense films with three different morphologies depending on the deposition method, which can be tuned based on specific needs. The film synthesized through sol-gel process exhibited a polycrystalline structure whereas the films synthesized via pulsed laser deposition exhibited columnar and epitaxial growth on Si and YSZ substrates, respectively. Therefore, we demonstrate that it is possible to make microstructure-tuned dense films while retaining the structure, chemical composition, valence states and band gap very similar to that observed in the powder form, thus paving the way to explore applications that require the bulk form with specific microstructures (such as columnar/epitaxial grains for SOFC applications and equiaxed microstructure for catalytic applications).

## CRediT authorship contribution statement

**M.K.** synthesized the materials and performed experiments and analysis. **L.V.** Performed experiments and analysis. **L.V., S.S.B.**, and **H.H.** conceived and supervised the project. All authors co-wrote and discussed the manuscript.

## Data availability

Data will be made available on request.

## Declaration of Competing Interest

The authors declare that they have no known competing financial interests or personal relationships that could have appeared to influence the work reported in this paper.

## Acknowledgements

Mohana V. Kante, Leonardo Velasco Estrada, and Horst Hahn are grateful for the support provided by Deutsche Forschungsgemeinschaft (Project no. HA 1344/45-1, VE 1111/1-1, 424789449). Subramshu S. Bhattacharya is grateful for the support provided by Indo-German DST-DFG collaborative project number DST/INT/DFG/P-01/2019 under the project identifier number 424789449. Leonardo Velasco thanks Karlsruhe Nano Micro Facility and Prof. Christian Kübel for the use of TEM at KIT.

## Appendix A. Supporting information

Supplementary data associated with this article can be found in the online version at doi:10.1016/j.jallcom.2023.169430.

## References

[1] A. Sarkar, B. Breitung, H. Hahn, High entropy oxides: the role of entropy, enthalpy and synergy, Scr. Mater. 187 (2020) 43–48.
[2] C.M. Rost, E. Sachet, T. Borman, A. Moballegh, E.C. Dickey, D. Hou, et al., Entropy-stabilized oxides, Nat. Commun. (2015) 6.
[3] A. Sarkar, C. Loho, L. Velasco, T. Thomas, S.S. Bhattacharya, H. Hahn, et al., Multicomponent equiatomic rare earth oxides with a narrow band gap and associated praseodymium multivalency, Dalton Trans. 46 (36) (2017) 12167–12176.
[4] L. Velasco, J.S. Castillo, M.V. Kante, J.J. Olaya, P. Friederich, H. Hahn, et al., Phase–property diagrams for multicomponent oxide systems toward materials libraries, Adv. Mater. 33 (43) (2021) 2102301, , https://doi.org/10.1002/adma.202102301
[5] A. Sarkar, P.K. Mannava, L. Velasco, C. Das, B. Breitung, S.S. Bhattacharya, et al., Determining role of individual cations in high entropy oxides: structure and reversible tuning of optical properties, Scr. Mater. (2022) 207.
[6] T.X. Nguyen, J. Patra, J.K. Chang, J.M. Ting, High entropy spinel oxide nanoparticles for superior lithiation–delithiation performance, J. Mater. Chem. A Mater. 8 (36) (2020) 18963–18973.
[7] J. Dąbrowa, M. Stygar, A. Mikuła, A. Knapik, K. Mroczka, W. Tejchman, et al., Synthesis and microstructure of the (Co,Cr,Fe,Mn,Ni)3O4 high entropy oxide characterized by spinel structure, Mater. Lett. 216 (2018) 32–36.
[8] H. Chen, N. Qiu, B. Wu, Z. Yang, S. Sun, Y. Wang, A new spinel high-entropy oxide (Mg0.2Ti0.2Zn0.2Cu0.2Fe0.2)3O4 with fast reaction kinetics and excellent stability as an anode material for lithium ion batteries, RSC Adv.. 10 (16) (2020) 9736–9744.
[9] A. Sarkar, R. Djenadic, D. Wang, C. Hein, R. Kautenburger, O. Clemens, et al., Rare earth and transition metal based entropy stabilised perovskite type oxides, J. Eur. Ceram. Soc. 38 (5) (2018) 2318–2327.
[10] T. Maiti, R. Banerjee, S. Chatterjee, M. Ranjan, T. Bhattacharya, S. Mukherjee, et al., High-entropy perovskites: an emergent class of oxide thermoelectrics with ultralow thermal conductivity, ACS Sustain Chem. Eng. 8 (46) (2020) 17022–17032, https://doi.org/10.1021/acssuschemeng.0c03849
[11] B. Matović, D. Zagorac, I. Cvijović-Alagić, J. Zagorac, S. Butulija, J. Erčić, et al., Fabrication and characterization of high entropy pyrochlore ceramics, Bol. De. la Soc. Esp. De. Cerám. Y. Vidr. (2021).
[12] Z. Teng, L. Zhu, Y. Tan, S. Zeng, Y. Xia, Y. Wang, et al., Synthesis and structures of high-entropy pyrochlore oxides, J. Eur. Ceram. Soc. 40 (4) (2020) 1639–1643.
[13] B. Jiang, C.A. Bridges, R.R. Unocic, K.C. Pitike, V.R. Cooper, Y. Zhang, et al., Probing the local site disorder and distortion in pyrochlore high-entropy oxides, J. Am. Chem. Soc. 143 (11) (2021) 4193–4204, https://doi.org/10.1021/jacs.0c10739
[14] Wang J., Cui Y., Wang Q., Wang K., Huang X., Stenzel D., et al., Lithium containing layered high entropy oxide structures, Sci. Rep., 2020,10(1), 1–13. ⟨https://www.nature.com/articles/s41598–020-75134–1⟩. (Accessed 19 January 2022).
[15] S.H. Albedwawi, A. AlJaberi, G.N. Haidemenopoulos, K. Polychronopoulou, High entropy oxides-exploring a paradigm of promising catalysts: a review, Mater. Des. 202 (2021).
[16] A. Sarkar, L. Velasco, D. Wang, Q. Wang, G. Talasila, L. de Biasi, et al., High entropy oxides for reversible energy storage, Nat. Commun. 9 (1) (2018) 1–9.
[17] A. Sarkar, R. Kruk, H. Hahn, Magnetic properties of high entropy oxides, Dalton Trans. 50 (6) (2021) 1973–1982.
[18] T. Maiti, R. Banerjee, S. Chatterjee, M. Ranjan, T. Bhattacharya, S. Mukherjee, et al., High-entropy perovskites: an emergent class of oxide thermoelectrics with ultralow thermal conductivity, ACS Sustain Chem. Eng. [Internet]. 8 (46) (2020) 17022–17032, https://doi.org/10.1021/acssuschemeng.0c03849
[19] A. Mao, H.Z. Xiang, Z.G. Zhang, K. Kuramoto, H. Yu, S. Ran, Solution combustion synthesis and magnetic property of rock-salt (Co0.2Cu0.2Mg0.2Ni0.2Zn0.2)O high-entropy oxide nanocrystalline powder, J. Magn. Magn. Mater. 484 (2019) 245–252.
[20] F. Okejiri, Z. Zhang, J. Liu, M. Liu, S. Yang, S. Dai, Room-temperature synthesis of high-entropy perovskite oxide nanoparticle catalysts through ultrasonication-based method, ChemSusChem 13 (1) (2020) 111–115, https://doi.org/10.1002/cssc.201902705
[21] M. Biesuz, L. Spiridigliozzi, G. Dell'Agli, M. Bortolotti, V.M. Sglavo, Synthesis and sintering of (Mg, Co, Ni, Cu, Zn)O entropy-stabilized oxides obtained by wet chemical methods, J. Mater. Sci. 53 (11) (2018) 8074–8085, https://doi.org/10.1007/s10853-018-2168-9
[22] H. Chen, W. Lin, Z. Zhang, K. Jie, D.R. Mullins, X. Sang, et al., Mechanochemical synthesis of high entropy oxide materials under ambient conditions: dispersion of catalysts via entropy maximization, ACS Mater. Lett. 1 (1) (2019) 83–88.
[23] A. Sarkar, R. Djenadic, N.J. Usharani, K.P. Sanghvi, V.S.K. Chakravadhanula, A.S. Gandhi, et al., Nanocrystalline multicomponent entropy stabilised transition metal oxides, J. Eur. Ceram. Soc. 37 (2) (2017) 747–754.
[24] D. Bérardan, S. Franger, A.K. Meena, N. Dragoe, Room temperature lithium superionic conductivity in high entropy oxides, J. Mater. Chem. A Mater. [Internet] 4 (24) (2016) 9536–9541 ⟨https://pubs.rsc.org/en/content/articlehtml/2016/ta/c6ta03249d⟩.
[25] A.D. Dupuy, X. Wang, J.M. Schoenung, Entropic phase transformation in nanocrystalline high entropy oxides, Mater. Res Lett. 7 (2) (2019) 60–67 ⟨https://www.tandfonline.com/action/journalInformation?journalCode=tmrl20⟩.
[26] R.K. Patel, S.K. Ojha, S. Kumar, A. Saha, P. Mandal, J.W. Freeland, et al., Epitaxial stabilization of ultra thin films of high entropy perovskite, Appl. Phys. Lett. [Internet] 116 (7) (2019), ⟨http://arxiv.org/abs/1911.03866⟩.
[27] N.A. Mohd Fadzil, M.H. Ab Rahim, G. Pragas Maniam, Brief review of ceria and modified ceria: synthesis and application, Mater. Res Express 5 (8) (2018) 085019, , https://doi.org/10.1088/2053-1591/aad2b5 ⟨https://iopscience.iop.org/article/⟩.
[28] Trovarelli A. , Catalysis by Ceria and Related Materials, 2002, 2. ⟨https://books.google.com/books/about/Catalysis_By_Ceria_And_Related_Materials.html?id=ve63CgAAQBAJ⟩. (Accessed 19 January 2022).
[29] N. Jaiswal, K. Tanwar, R. Suman, D. Kumar, S. Uppadhya, O. Parkash, A brief review on ceria based solid electrolytes for solid oxide fuel cells, J. Alloy. Compd. 781 (2019) 984–1005.
[30] Y.P. Lan, H.Y. Sohn, Effect of oxygen vacancies and phases on catalytic properties of hydrogen-treated nanoceria particles, Mater. Res Express 5 (3) (2018) 035501, , https://doi.org/10.1088/2053-1591/aaaff4
[31] Jung G.B., Huang T.J., Chang C.L. , Effect of Temperature and Dopant Concentration on the Conductivity of Samaria-doped Ceria Electrolyte.
[32] R. Djenadic, A. Sarkar, O. Clemens, C. Loho, M. Botros, V.S.K. Chakravadhanula, et al., Multicomponent equiatomic rare earth oxides, Mater. Res Lett. 5 (2) (2017) 102–109, https://doi.org/10.1080/21663831.2016.1220433
[33] S. Kazlauskas, A. Kežionis, T. Šalkus, A.F. Orliukas, Effect of sintering temperature on electrical properties of gadolinium-doped ceria ceramics, J. Mater. Sci. 50 (8) (2015) 3246–3251, https://doi.org/10.1007/s10853-015-8892-5
[34] S.I. Ahmad, P. Koteshwar Rao, I.A. Syed, Sintering temperature effect on density, structural and morphological properties of Mg- and Sr-doped ceria, J. Taibah Univ. Sci. 10 (3) (2016) 381–385.
[35] H. Yoshida, K. Miura, J.I. Fujita, T. Inagaki, Effect of gallia addition on the sintering behavior of Samaria-doped ceria, J. Am. Ceram. Soc. 82 (1) (1999) 219–221, https://doi.org/10.1111/j.1151-2916.1999.tb01747.x
[36] Kou S. , Welding Metallurgy. Welding Metallurgy, 2002. https://onlinelibrary.wiley.com/doi/book/10.1002/0471434027. (Accessed 6 July 2022).
[37] R. Sinclair, S.C. Lee, Y. Shi, W.C. Chueh, Structure and chemistry of epitaxial ceria thin films on yttria-stabilized zirconia substrates, studied by high resolution electron microscopy, Ultra 176 (2017) 200–211.
[38] T. Ami, Y. Ishida, N. Nagasawa, A. Machida, M. Suzuki, Room-temperature epitaxial growth of CeO2(001) thin films on Si(001) substrates by electron beam evaporation, Appl. Phys. Lett. 78 (10) (2001) 1361, https://doi.org/10.1063/1.1351849
[39] Dubbink D., Koster G., Rijnders G. , Growth mechanism of epitaxial YSZ on Si by pulsed laser deposition, Sci. Rep., 2018, 8(1), 1–10. ⟨https://www.nature.com/articles/s41598–018-24025–7⟩. (Accessed 12 April 2022).
[40] A. Mazor, D.J. Srolovitz, P.S. Hagan, B.G. Bukiet, Columnar growth in thin films, Phys. Rev. Lett. 60 (5) (1988) 424–427.
[41] J.E. Prieto, I. Markov, Stranski–Krastanov mechanism of growth and the effect of misfit sign on quantum dots nucleation, Surf. Sci. 664 (2017) 172–184.
[42] W. Choi, T. Sands, Effect of oxygen partial pressure during pulsed laser deposition on the orientation of CeO2 thin films grown on (100) silicon, J. Mater. Res. 18 (8) (2003) 1753–1756, https://doi.org/10.1557/JMR.2003.0242
[43] S. Lütkehoff, M. Neumann, A. Lebarski, 3*d* and 4*d* x-ray-photoelectron spectra of Pr under gradual oxidation, Phys. Rev. B 52 (19) (1995) 13808, https://doi.org/10.1103/PhysRevB.52.13808
[44] Yamada T., Wakiya N., Shinozaki K., Mizutani N. , Effects of Oxygen Partial Pressure and Laser Energy Density on the Heteroepitaxial Growth of YSZ on Si (001) by Pulsed Laser Deposition.

[45] A. Sarkar, B. Eggert, L. Velasco, X. Mu, J. Lill, K. Ollefs, et al., Role of intermediate 4f states in tuning the band structure of high entropy oxides, APL Mater. 8 (5) (2020) 051111, , https://doi.org/10.1063/5.0007944
[46] F. Gunkel, D. v Christensen, Y.Z. Chen, N. Pryds, Oxygen vacancies: the (in)visible friend of oxide electronics, Appl. Phys. Lett. 116 (12) (2020).
[47] D.R. Ou, T. Mori, F. Ye, J. Zou, G. Auchterlonie, J. Drennan, Oxygen-vacancy ordering in lanthanide-doped ceria: dopant-type dependence and structure model, Phys. Rev. B Condens Matter Mater. Phys. 77 (2) (2008) 024108, , https://doi.org/10.1103/PhysRevB.77.024108
[48] L.A.J. Garvie, P.R. Buseck, Determination of Ce4+/Ce3+ in electron-beam-damaged CeO2 by electron energy-loss spectroscopy, J. Phys. Chem. Solids 60 (12) (1999) 1943–1947.
[49] J.A. Fortner, E.C. Buck, The chemistry of the light rare-earth elements as determined by electron energy loss spectroscopy, Appl. Phys. Lett. 68 (26) (1996) 3817–3819.
[50] C.M. Sims, R.A. Maier, A.C. Johnston-Peck, J.M. Gorham, V.A. Hackley, B.C. Nelson, Approaches for the quantitative analysis of oxidation state in cerium oxide nanomaterials, Nanotechnology 30 (8) (2019).
[51] E. Paparazzo, On the curve-fitting of XPS Ce(3d) spectra of cerium oxides, Mater. Res Bull. 46 (2) (2011) 323–326.
[52] E. Bêche, P. Charvin, D. Perarnau, S. Abanades, G. Flamant, Ce 3d XPS investigation of cerium oxides and mixed cerium oxide (Ce xTiyOz), Surf. Interface Anal. 40 (3–4) (2008) 264–267.
[53] C. Barth, C. Laffon, R. Olbrich, A. Ranguis, P. Parent, M. Reichling, A perfectly stoichiometric and flat CeO2 (111) surface on a bulk-like ceria film, Sci. Rep. (2016) 6.
[54] H. Borchert, Y. v Frolova, V. v Kaichev, I.P. Prosvirin, G.M. Alikina, A.I. Lukashevich, et al., Electronic and chemical properties of nanostructured cerium dioxide doped with praseodymium, J. Phys. Chem. B 109 (12) (2005) 5728–5738.
[55] A. Bianconi, A. Kotani, K. Okada, R. Giorgi, A. Gargano, A. Marcelli, et al., Many-body effects in praesodymium core-level spectroscopies of < span class, Phys. Rev. B 38 (5) (1988) 3433, https://doi.org/10.1103/PhysRevB.38.3433
[56] J.J. Kim, S.R. Bishop, D. Chen, H.L. Tuller, Defect chemistry of Pr doped ceria thin films investigated by in situ optical and impedance measurements, Chem. Mater. 29 (5) (2017) 1999–2007.
[57] S.R. Bishop, T.S. Stefanik, H.L. Tuller, Electrical conductivity and defect equilibria of Pr0.1Ce 0.9O2-δ, Phys. Chem. Chem. Phys. 13 (21) (2011) 10165–10173.
[58] Gödickemeier M. , Mixed Ionic Electronic Conductors for Solid Oxide Fuel Cells, 1996. https://doi.org/10.3929/ethz-a-001608299. (Accessed 21 January 2022).
[59] S. Hong, D. Lee, Y. Lim, J. Bae, Y.B. Kim, Yttria-stabilized zirconia thin films with restrained columnar grains for oxygen ion conducting electrolytes, Ceram. Int 42 (15) (2016) 16703–16709.
[60] M.V.F. Schlupp, B. Scherrer, H. Ma, J.G. Grolig, J. Martynczuk, M. Prestat, et al., Influence of microstructure on the cross-plane oxygen ion conductivity of yttria stabilized zirconia thin films, Phys. Status Solidi (a) 209 (8) (2012) 1414–1422, https://doi.org/10.1002/pssa.201228248
[61] J.H. Joo, G.M. Choi, Electrical conductivity of YSZ film grown by pulsed laser deposition, Solid State Ion. 177 (11–12) (2006) 1053–1057.
[62] Z. Hou, W. Pei, X. Zhang, K. Zhang, Y. Liu, J. Deng, et al., Rare earth oxides and their supported noble metals in application of environmental catalysis, J. Rare Earths 38 (8) (2020) 819–839.
[63] R.J. Gorte, Ceria in catalysis: From automotive applications to the water–gas shift reaction, AIChE J. 56 (5) (2010) 1126–1135, https://doi.org/10.1002/aic.12234
[64] J. Paier, C. Penschke, J. Sauer, Oxygen defects and surface chemistry of ceria: quantum chemical studies compared to experiment, Chem. Rev. 113 (6) (2013) 3949–3985, https://doi.org/10.1021/cr3004949